1 # Regional uncertainty of GOSAT XCO$_2$ retrievals in China:
2 # Quantification and attribution

3

4 Nian Bie[1, 2], Lipping Lei[1], Zhaocheng Zeng[3], Bofeng Cai[4], Shaoyuan Yang[1, 2], Zhonghua He[1, 2],
5 Changjiang Wu[1, 2], and Ray Nassar[5]
6 [1]Key Laboratory of Digital Earth Science, Institute of Remote Sensing and Digital Earth, Chinese Academy of Sciences,
7 Beijing 100094, China
8 [2]University of Chinese Academy of Sciences, Beijing 100049, China
9 [3]Division of Geological and Planetary Sciences, California Institute of Technology, Pasadena, CA91125, USA
10 [4]The Center for Climate Change and Environmental Policy, Chinese Academy for Environmental Planning, Ministry of
11 Environmental Protection, Beijing, 100012, China
12 [5]Climate Research Division, Environment and Climate Change Canada

13 *Correspondence to*: leilp@radi.ac.cn

14 **Abstract**. The regional uncertainty of XCO$_2$ (column-averaged dry air mole fraction of CO$_2$) retrieved using different

15 algorithms from the Greenhouse gases Observing SATellite (GOSAT) and its attribution are still not well understood. This

16 paper investigates the regional performance of XCO$_2$ within a band of 37°N~ 42°N segmented into 8 cells in a grid of 5°

17 from west to east (80°E ~120°E) in China, where there are typical land surface types and geographic conditions. The former

18 include the various land covers of desert, grassland and built-up areas mixed with cropland, and the latter include

19 anthropogenic emissions that tend to be small to large from west to east, including those from the megacity of Beijing. For

20 these specific cells, we evaluate the regional uncertainty of GOSAT XCO$_2$ retrievals by quantifying and attributing the

21 consistency of XCO$_2$ retrievals from five algorithms (ACOS, NIES, EMMA, OCFP, and SRFP) by intercomparison and

22 particularly by comparing these with simulated XCO$_2$ from the Goddard Earth Observing System 3-D chemical transport

23 model (GEOS-Chem), the nested model in East Asia. We introduce the anthropogenic CO$_2$ emissions data generated from

24 the investigation of surface emitting point sources that was conducted by the Ministry of Environmental Protection of China

25 to GEOS-Chem simulations of XCO$_2$ over the Chinese mainland. The results indicate that (1) regionally, the five algorithms

26 demonstrate smaller absolute biases between 0.9-1.5 ppm in eastern cells, which are covered by built-up areas mixed with

27 cropland with intensive anthropogenic emissions, than those in the western desert cells with a high-brightness surface, 1.2-

28 2.2 ppm from the pairwise comparison results of XCO$_2$ retrievals. The inconsistency of XCO$_2$ from the five algorithms tends

29 to be high in the Taklimakan Desert in western cells, which is likely induced by high surface albedo in addition to dust

30 aerosols in this region. (2) Compared with XCO$_2$ simulated by GEOS-Chem (GEOS-XCO$_2$), the XCO$_2$ values of ACOS and

31 SRFP better agree with GEOS-XCO$_2$, while OCFP is the least consistent with GEOS-XCO$_2$. (3) Viewing attributions of

32 XCO$_2$ in the spatio-temporal pattern, ACOS, SRFP and EMMA demonstrate similar patterns, while OCFP is largely

33 different from the others. In conclusion, the discrepancy in the five algorithms is the smallest in eastern cells in the

34 investigated band where the megacity of Beijing is located and where there are strong anthropogenic CO$_2$ emissions, which

Atmospheric
Measurement
Techniques
Discussions

35   implies that XCO_2 from satellite observations could be reliably applied in the assessment of atmospheric CO_2 enhancements

36   induced by anthropogenic CO_2 emissions. The large inconsistency among the five algorithms presented in western deserts

37   with a high albedo and dust aerosols, moreover, demonstrates that further improvement is still necessary in such regions,

38   even though many algorithms have endeavored to minimize the effects of aerosols and albedo.

39

40   Key words: GOSAT, XCO_2 retrieval algorithms, simulated XCO_2 by GEOS-Chem, regional uncertainty, anthropogenic

41   emission, and desert

42   **1 Introduction**

43   The column-averaged dry air mole fraction of CO_2 (XCO_2) derived from satellite observations, such as the SCanning

44   Imaging Absorption spectroMeter of Atmospheric CHartographY (SCIAMACHY) (Burrows et al., 1995; Bovensmann et al.,

45   1999) , the Greenhouse gases Observing SATellite (GOSAT) (Yokoda et al., 2004), Orbiting Carbon Observatory (OCO-2)

46   (Crisp et al., 2004), and Chinese Carbon Satellite (TanSat) (Liu et al., 2013), have largely improved our understanding of

47   the variation in atmospheric CO_2 concentration and carbon sources and sinks at a global and regional scale. There have been

48   several full-physics retrieval algorithms specially developed for retrieving XCO_2 from the GOSAT spectrum, mainly

49   including the NASA Atmospheric CO_2 Observations from Space (ACOS) (O'Dell et al., 2012), the National Institute for

50   Environmental Studies (NIES) (Yoshida et al., 2013), University of Leicester full-physics XCO_2 (OCFP) (Cogan et al., 2012)

51   and RemoTeC XCO_2 Full Physics (SRFP) (Butz et al., 2011). Additionally, the ensemble median algorithm EMMA was put

52   forward as a combination of retrieval products from independent algorithms including ACOS, NIES, OCFP, and SRFP

53   (Reuter et al., 2013).

54   Satellite-retrieved XCO_2 is susceptible to the effects of the light path, observed spectrum, surface states, and so

55   on(O'Dell et al., 2012; Oshchepkov et al., 2013).The bias and performance of XCO_2 from an algorithm could change in

56   different regions with differing land surfaces and anthropogenic emissions. Spatio-pattern attributions of XCO_2 viewed from

57   different algorithms are also different, even in the same region, due to the different physical approaches of the algorithms,

58   assumptions of atmospheric conditions (aerosol, surface pressure, CO_2 profile, etc.), and pre- and post-processing filters. To

59   date, the validation of XCO_2 retrievals from these algorithms focuses on using ground-based measurements from Total

60   Carbon Column Observing Network (TCCON) sites (Wunch et al., 2011; Yoshida et al., 2013; Hewson, 2016; Buchwitz et

61   al., 2015, Detmers et al., 2015, Oshchepkov et al., 2013) and their consistency evaluation and cross-comparison both at a

62   global scale and in continental regions (Kulawik et al., 2016; Lindqvist et al., 2015; Lei et al., 2014).The precision and

63   uncertainty of satellite-retrieved XCO_2 outside TCCON stations, most of which are located remote from abundant biosphere

64   fluxes and human activities, are still not well evaluated. The sparseness of TCCON stations over the globe, moreover, means

65   a lack of enough ground observations to validate satellite retrievals. Specifically, there are no good TCCON data available in

66   China, and only a few satellite retrievals were validated using ground-based Fourier Transform Spectrometer (FTS) XCO_2

Atmospheric
Measurement
Techniques
Discussions

67 measurements in Hefei (Wang et al., 2016). In the analysis and application of XCO_2 data from ACOS, NIES, OCFP, SRFP

68 and EMMA, we found that unreasonably high XCO_2 was demonstrated in the Taklimakan desert in China (Bie et al., 2016;

69 Liu et al., 2015). For this reason, we extended the scope to select a larger study period and to further assess the overall

70 performance of these five algorithms at a regional scale.

71   With the advantage of continuity in space and time, atmospheric transport model simulation of CO_2 has been widely

72 used in assessing the performance of satellite-retrieved XCO_2 (Cogan et al., 2012; Lindqvist et al., 2015; Kulawik et al.,

73 2016). As anthropogenic emission of CO_2 is the major contributor to increases of CO_2 in the atmosphere, many studies have

74 been involved in deriving estimates of anthropogenic CO_2 emissions (Oda et al., 2011; Andres et al., 2011). It is known that

75 there exists high uncertainty in estimates of CO_2 emissions from both the burning of fossil fuel and cement production (FF

76 CO_2 emissions) throughout China (Guan et al., 2012; Liu et al., 2015). As noted by Andrews et al. (2012), there exist many

77 kinds of restrictions (e.g., commercial competitiveness reasons) in obtaining accurate data on sub-national (e.g., large-point-

78 source or provincial) FF CO_2 emissions. Furthermore, the assumption of uniform per-capita emissions within a country has

79 also been shown to be unreliable for large countries with diversified economies and electricity-generation methods (Nassar et

80 al., 2013). In the previous study of Keppel-Aleks (2013), the simulated Chinese XCO_2 data was increased by a national

81 uniform ratio for the corresponding XCO_2 contributed by fossil sources to account for the underestimation in Chinese

82 emissions, in which way the spatial variability of Chinese FF emissions was not considered sufficient.

83   In this paper, we focus on a latitude band of 37°N-42°N from 80°E to 120°E in China, where there are various typical

84 land covers such as desert, including the Taklimakan desert, and grassland and built-up areas mixed with croplands,

85 including the megacity of Beijing, and there are anthropogenic emissions that trend from small amounts to large amounts

86 from west to east. In this band, the inconsistencies of XCO_2 values derived from five algorithms including ACOS V3.5,

87 NIES V02.21, OCFP 6.0, SRFP V2.3.7, and EMMA V2.1c are compared and evaluated in this paper. Moreover, a forward

88 model simulation data set from GEOS-Chem is also used for intercomparison. To improve the simulation of CO2

89 concentration, we introduced a new emission data set, the Chinese High Resolution Emission Gridded Data (CHRED),

90 which is produced by the Ministry of Environmental Protection, China (MEP) based on investigations of emitting point

91 sources from approximately 150 million enterprises throughout the country in 2012 (Wang et al., 2014; Cai et al., 2014).

92   First, we aim to reveal the regional uncertainty of XCO_2 observed by GOSAT for the different land covers and

93 anthropogenic CO_2 emission regions through the inconsistency of five algorithms, and second, we aim to give a reasonable

94 and valuable reference for the analysis and application of XCO_2 data when using these XCO_2 data from the five algorithms.

95 Sec. 2 in this paper describes the XCO_2 retrievals data from five algorithms and the implementation of XCO_2 simulated by

96 GEOS-Chem using CHRED. Inconsistencies of XCO_2 datasets among the five algorithms are quantified and evaluated as

97 follows: pairwise comparisons of XCO_2 between algorithms and comparisons with GEOS-Chem simulations in Sec. 3. The

98 spatio-temporal patterns of XCO_2 from each algorithm are investigated using a combination of sine and cosine trigonometric

99 functions to fit monthly averaged XCO_2 from March 2010 to February 2013 in Sec. 4. Furthermore, the most likely

100 attribution-affecting factors on regional inconsistency, including aerosol and surface albedo, are described in Sec. 5. The

Atmospheric
Measurement
Techniques
Discussions

101 latest ACOS V7.3 dataset, moreover, is also evaluated by cross-comparisons with GEOS-Chem and other algorithms

102 including ACOS V3.5, NIESV02.XX, OCFP V6.0, SRFP V2.3.7 and EMMA v2.1.C, as shown in subsections of Sec. 5.

103 Finally, the regional performances of five algorithms and the regional uncertainty of GOSAT XCO2 retrievals from the

104 results above are summarized, and conclusions are given in Sec. 6.

105 2 Study area and data

106 2.1 Study area

107 The latitude band of 37°N~42°N from 80°E to 120°E in China is selected as the study area, which is segmented into eight

108 cells in a grid of 5°×5° units for comparison and evaluation. The study area has two typical surface characteristics as shown

109 in Fig. 1, supporting our assessment of the performance of XCO_2 retrievals from five algorithms: (1) the difference of

110 anthropogenic CO_2 emissions from west to east is significant going from small amounts to large amounts as shown in Fig.

111 1(left), where data are from the Open-source Data Inventory for Anthropogenic CO_2 (ODIAC), a global annual fossil fuel

112 CO_2 emission inventory developed by combining a worldwide point-source database and satellite observations of the global

113 nightlight distribution (Oda et al., 2011). There are almost no anthropogenic CO_2 emissions in the western cells ending at

114 105°E, while there is high anthropogenic emission located in the cells on the eastern end. (2) There are typical land covers

115 from west to east mainly composed of desert (sand in two cells from 80°E to 90°E, Gobi in two cells from 90°E to 100°E,

116 sand in a cell from 100°E to 105°E), grassland in a cell from 105 to 110°E, and cropland and built-up areas in two cells from

117 110°E to 120°E as shown in Fig. 1 (right). These characteristics may bring about complicated aerosol composition and

118 concentration. One of the main reasons for focusing on this band, however, is the greater availability of high-quality GOSAT

119 scans in this area compared to other areas in China.
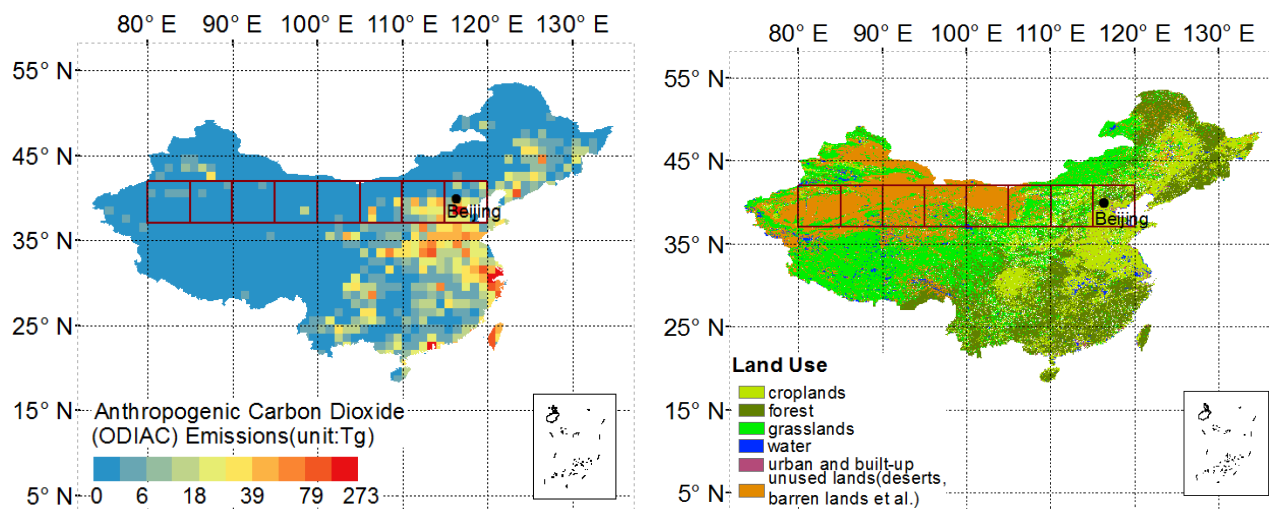
Fig. 1. Location of the study area segmented into cells (deep red cells) in China and annual fossil fuel CO_2 emission in 2012 (left) (1 x 1 degree) from ODIAC and land use mapping (right) in 2010, where the black dot represents Beijing, the capital of China.

2.2 GOSAT XCO_2 dataset derived from five algorithms

We collected XCO_2 data from March 2010 to February 2013 derived from five algorithms: ACOS V3.5 (http://CO2.jpl.nasa.gov), NIES V02.xx (RA version with GU screening scheme) (http://data.gosat.nies.go.jp/ GosatUserInterfaceGateway/ guig/GuigPage/ open.do?l ang=en), OCFP V6.0, SRFP V2.3.7 and EMMA V2.1c (http://www. esa- ghg-cci.org/ sites/ default/ files/ /documents/public/documents/GHG-CCI_DATA.html) , the version of EMMA without SCIAMACHY data included. The major characteristics of the five algorithms and the data sources are listed in Table 1. The validation at TCCON sites for all algorithms indicates that the bias is less than 1.2 ppm and that the standard deviation is less than 2.0 ppm. All algorithms take aerosol optical depth (AOD) into consideration in their data screening scheme but in slightly different manners. The recommended bias corrections are applied to the collected XCO_2 data from ACOS, OCFP and SRFP . Data observed with high gain and passing the corresponding recommended quality control are used in ACOS, NIES, OCFP and SRFP while all data from EMMA are used.

Atmospheric
Measurement
Techniques
Discussions

135   **Table 1 Summary of validating results, data screening schemes, bias corrections and consideration in scattering among algorithms.**

	ACOS	NIES	OCFP	SRFP	EMMA
Validation with TCCON*	0.3 ppm 1.7 ppm	-1.2 ppm 2.0 ppm	0.04 ppm 1.78ppm	0.01 ppm 1.93 ppm	0.28 ppm 1.9 ppm
Data screening scheme	Aerosol_total_aod: 0.015 to 0.25 Sounding_altitude:<3000 $0.55<XCO_2\_uncer<2.0$ ppm Aod_dust<0.15 The difference of the retrieved and priori surface pressure from the A-band cloud-screen $\triangle P_{s,cld}$:(-12,4.1) hPa	Retrieved aerosol optical thickness:<=0.1 Difference of retrieved and a priori surface pressure:<=20 hpa Blended albedo: <1	Retrieved type 1 (small) AOD: <=0.3 Retrieved type 2 (large) AOD: <=0.15 Retrieved ice type AOD: <=0.025 Error on retrieved XCO_2 :<=2.15	Aerosol optical thickness :<0.3 3<aero_size<5 0<aerosol_filter<300 Error on retrieved XCO_2: <1.2 ppm standard deviation of surface elevation within GOSAT ground pixel: <80m Blended albedo: <0.9	-
Consideration in scattering	4 extinction profiles (two aerosol types , water and ice cloud)	logarithms of the mass mixing ratios of fine-mode aerosols and coarse mode aerosols with aerosol optical properties based on SPRINTARS V3.84	Aerosol profile scaling of 2 different aerosol types; cloud extinction profile scaling	Aerosol particle number concentration, aerosol size parameter, aerosol height	-
Bias correction	$X'_{CO2} = X_{CO2} - 0.5 - 0.155 * (\Delta P_{s,cld} + 2.7) + 10.6 * (\alpha'_3 - 0.204) + 0.0146 * (\Delta GRAD_{CO2} - 35) + 12.8 * (AOD_{DUST} - 0.01)$	-	Via a regression analysis of the difference between GOSAT and TCCON XCO_2 land observations. See details in the product user guide	$X'_{CO2} = X_{CO2} * (1.002837 + 2.1176e - 5 * \phi)$ ϕ: the aerosol filter	-
Sources	Osterman et al., 2016; O'Dell et al., 2012; D.Wunch et al., 2011b.	NIES (GOSAT Project Office), 2015; Yoshida et al., 2013; D.Wunch et al., 2011b.	Hew, 2016; GHG-CCI group at University of Leicester, 2014.	Detmers et al., 2015; Hasekamp et al., 2015	Buchwitz et al. 2016. Reuter et al., 2013.

136   *The first represents mean biases, and the second represents overall standard deviations.**

137   Within the study area, the total numbers of valid GOSAT XCO_2 observations are 3345, 3556, 2282, 3685 and 2796 in

138   ACOS, NIES, OCFP, SRFP and EMMA, respectively. Figure 2 shows the number of available XCO_2 retrievals during the 4

139   seasons (spring: MAM; summer: JJA; autumn: SON; winter: DJF). It can be seen that the number of available XCO_2

140   retrievals is clearly smaller in spring and summer than that in autumn and winter due to different meteorological conditions

141   and data-screening processes. The cloudiness in spring and summer caused by the monsoon climate disturbs satellite

142   observation, while the smaller data number in the west of 110 °E is due to frequent dust storm in the Taklimakan Desert.
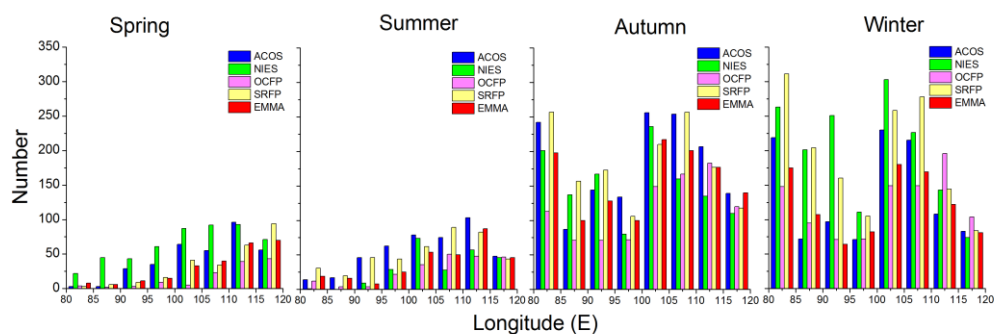

143

144   **Fig. 2. Number of single scans from five GOSAT-XCO_2 data sets over each 5x5 °cells in spring, summer, autumn and winter from**
145   **March 2010 to February 2013. Spring: MAM; summer: JJA; autumn: SON; winter: DJF.**

146   **2.3 XCO_2 simulations from GEOS-Chem**

147   We use GEOS-Chem version 10-01 driven by GEOS-5 and the details of the main input emissions are as follows: 1)

148   Fossil fuel fluxes are taken from ODIAC version 2013. On the other hand, we also introduce the new emission data set

149   CHRED for the Chinese mainland. 2) The balanced biosphere CO2 uptake and emission fluxes are taken from the Simple

150   Biosphere Model version 3 (SiB3) [Messerschmidt et al. 2012]. 3) Biomass emissions are taken from Global Fire Emission

151   Database version 4 (GFEDv4) (Giglio et al., 2013). 4) Ocean fluxes are taken as Takahashi et al. (2009) suggested. The input

152   emissions for the GEOS-Chem CO_2 simulation are described in Nassar et al. (2010), although we have used some of the

153   most recent updates available in the GEOS-Chem version 10-01 and the Harvard–NASA Emission Component version 1.0

154   (HEMCO) module (Keller et al., 2014), a versatile component for emissions in atmospheric models. Higher model resolution

155   is very important in the calculation of the concentrations of atmospheric gases, especially over land where topography

156   smoothing (compared to reality) is determined by horizontal resolution (Ciais et al., 2010). Considering this, GEOS-Chem at

157   0.5 °(latitude) x 0.666 °(longitude) horizontal resolution, the nested grid model in China, was taken for the CO_2 simulation

158   with boundary conditions provided by the global model at 2 °(latitude) x 2.5 °(longitude) resolution. We made a restart file

159   with 386.4 ppm for both the global simulation and the nested simulation on 1 January 2009 based on NOAA ESRL data.

160   Both the global model and the nested-grid model were run twice, driven by the same CO_2 fluxes from January 2009 to

161   February 2013 except that the ODIAC was chosen for the first run and CHRED for the second as the input fossil-fuel fluxes

162   over the Chinese mainland. With an average for local hours between 12 pm and 13:30 pm, model CO_2 profiles were

163 presented from January 2010 to February 2013, allowing sufficient time for the high-resolution model to adjust to transients

164 introduced by the initialization of the model on 1 January 2009. The pressure-weighting function described in Connor (2008)

165 was applied to translate level-based modeling CO_2 to XCO_2. Figure 3 presents the spatial difference of emissions over the

166 Chinese mainland between CHRED and ODIAC at a horizontal resolution of 1°x1°. The values of emissions are mostly

167 larger in CHRED than in ODIAC, as shown in Fig. 3, and this difference tends to be large in the eastern part of our study

168 area. In addition, the difference in their total emissions, 10.38 Pg CO_2 (CHRED) to 9.64 Pg CO_2 (ODIAC), is not small.

169 ODIAC is also found to exhibit an overestimation of emissions in large cities compared to CHRED.
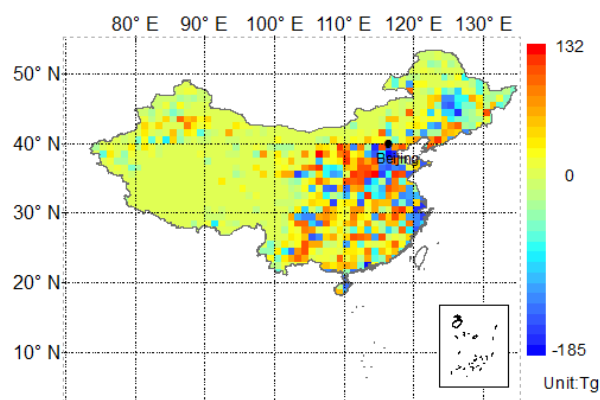

Fig. 3. Difference of annual total anthropogenic CO_2 emissions between CHRED and ODIAC in 2012 in China, where the black dot represents Beijing, the capital of China.

173 For each 1°x1° grid, the corresponding annual CO_2 emissions in the years from 2009 to 2012 were allocated by the ratio

174 of emissions in CHRED to that in ODIAC in 2012. We acquired the new input inventory of CO_2 emissions, CHRED, by

175 scaling the obtained yearly emissions with the ratio of monthly emissions to the yearly ones in ODIAC. In this way, we have

176 altered the spatial and temporal distribution, but not at temporal scales finer than monthly. This is expected to be an

177 improvement upon the current ODIAC emission values.

178 The annually averaged XCO_2 driven by both CHRED and ODIAC are calculated and shown in Fig. 4. The impact of

179 emission deviations of CHRED from ODIAC is significant, with an average XCO_2 increase of 0.7 ppm over China. There

180 are also obvious differences in spatial patterns, especially in Northwest China, Northeast China, North China and South

181 China. Modeling CO_2 from CHRED increases values up to 0.7 ppm in most parts east of 100°E with a maximum at 1.4

182 ppm compared to that from ODIAC. The increase in the annual mean, which should not be ignored, is approximately 1 ppm

183 east of 110°E in the latitude zone of 37°N~ 42°N. Modeling the XCO_2 data set from CHRED is used to compare with

184 satellite-retrieved XCO_2 in our following experiment.
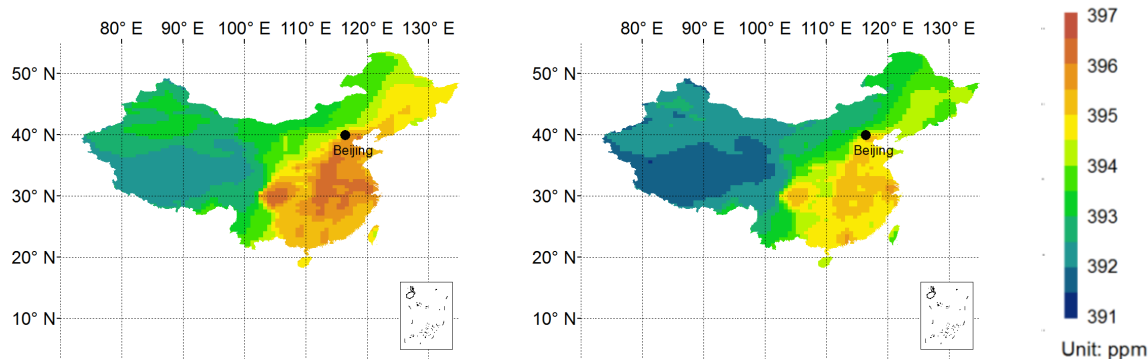
Fig. 4. The annual mean XCO_2 concentrations driven by CHRED (left) and by ODIAC (right) in 2012 with GEOS-Chem in China, where the black dot represents Beijing, the capital of China.

2.4 Aerosol optical depth and surface albedo data

The monthly mean aerosol data was collected from the NASA Earth Observing System's Multi-angle Imaging Spectro-radiometer (MISR) Level 3 Component Global Aerosol Product, downloaded from the website https://eosweb.larc.nasa.gov/project/misr. The released GLASS (Glass Land Surface Satellites) albedo is used, which is a gapless, long-term continuous and self-consistent data-set with accuracy similar to that of the Moderate Resolution Imaging Spectrometer (MODIS) MCD43 product (Liu et al., 2013). Data were downloaded from the website http://glcf.umd.edu/data/abd/.

3 Quantification of agreement of XCO_2 retrievals from five algorithms in the same footprints

We focus on the difference of each footprint XCO_2 retrieval in this section. Comparison of XCO_2 from the five algorithms with GEOS-Chem simulations driven by CHRED, and pairwise comparisons of XCO_2 between algorithms were calculated as a quantified indicator of their differences.

3.1 Comparisons with GEOS-Chem simulations

We used the nested GEOS-Chem simulation XCO_2 as a baseline to quantify the regional consistency of the five algorithms. Our output model CO_2 profile is the averaged concentration during the local hours 12:00-13:30 pm corresponding to the local time of overpass and locations (latitude and longitude) of GOSAT. To compare XCO_2 retrievals from ACOS, NIES, OCFP, SRFP and EMMA, corresponding GEOS-Chem XCO_2 data were created by applying averaging kernels from each algorithm to model CO_2 profiles as suggested by Rodgers (2003). Correlation diagrams of XCO_2 between GEOS-Chem (X) and GOSAT (Y) for the five algorithms are shown in Fig. 5. The regression slope (a), the coefficient of determination (R^2), the correlation coefficient (r), and biases of GOSAT (Y) from GEOS-Chem(X) are also shown in the inset of each panel.

It can be found that the linear fits and the correlations with GEOS-Chem are better for ACOS, OCFP and EMMA (R^2 approximately 0.66) than for either NIES or SRFP (R^2 approximately 0.59). The regression slope is the closest to unity in the

208   OCFP panel (0.94), which means the best similarity in variation. The slope of GEOS-Chem vs ACOS ranks second (a=0.87)

209   while it is less than 0.8 vs NIES and SRFP. The bias relative to GEOS-Chem is within 0.5 ppm for ACOS, SRFP, and

210   EMMA, while it is 2 ppm and 1.2 ppm for NIES and OCFP, respectively.

211
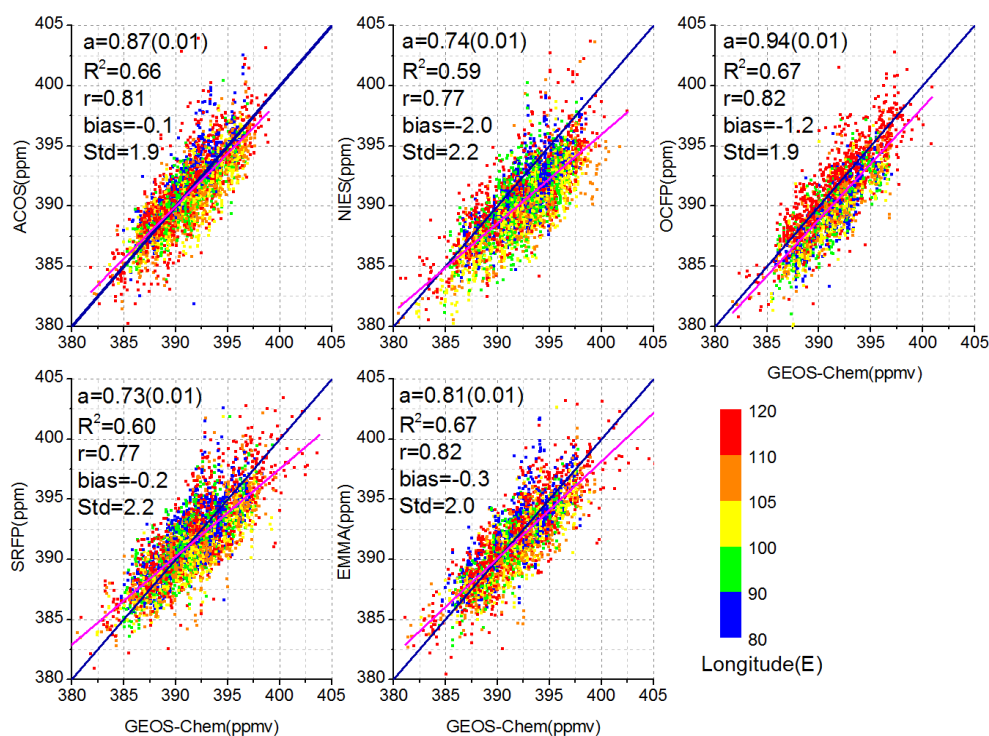
Fig. 5: Correlation diagrams of GOSAT XCO$_2$ (Y) for the five algorithms versus GEOS-Chem (X) XCO$_2$ and linear fit statistics (insets of panels). GEOS-Chem data are selected corresponding to locations and time of XCO$_2$ from the five algorithms in cells. Deep blue solid lines represent a 1:1 line, and the magenta lines demonstrate the best fit for all observations. Colored points represent XCO$_2$ for different cells: blue-[80 °E, 90 °E], green-[90 °E, 100 °E], yellow-[100 °E, 105 °E], orange-[105 °E, 110 °E], and red-[110 °E, 120 °E] in the latitude zone [37 °N, 42 °N].

217   Table 2 shows the biases and number of samples used between each algorithm and GEOS-Chem in each cell. It can be

218   seen that the biases relative to GEOS-Chem in all cells are below 1 ppm for ACOS, SRFP and EMMA, which implies better

219   consistency with GEOS-Chem regionally than NIES and OCFP. NIES presents values 1.2-3.1 ppm lower than GEOS-Chem

220   in all cells excluding the cell of 115 °E, which is because no corrections were implemented to reduce the existing systematic

221   biases in the NIES data set (Yoshida et al., 2013). The bias of OCFP relative to GEOS-Chem is larger than 1.2 ppm toward

222   the west of 110 °E, while it is 0.1 ppm toward the east of 110 °E. The standard deviations of the five algorithms with GEOS-

223   Chem range from 1.4 ppm to 2.7 ppm in all cells.

224

Atmospheric
Measurement
Techniques
Discussions

225 **Table 2. The biases relative to GEOS-Chem for five algorithms in each cell. The values in parentheses are the biases and their**
226 **standard deviations (upper values) and the number of samples (lower values) for each algorithm.**

| Left longitude of cells(°E)	80	85	90	95	100	105	110	115
ACOS	0.7(1.6)	0.5(1.6)	-0.4(1.4)	-0.3(1.5)	-0.7(1.7)	-0.7(1.7)	0.0(2.2)	0.5(2.1)
	478	179	316	303	629	599	515	326
NIES	**-1.4**(1.7)	**-1.6**(1.8)	**-1.6**(1.8)	**-2.3**(2.5)	**-3.0**(1.9)	**-3.1**(2.2)	**-1.6**(2.5)	-0.7(2.4)
	487	383	470	281	700	506	428	301
OCFP	**-1.8**(1.4)	**-1.8**(1.5)	**-2.2**(1.4)	**-1.2**(2.0)	**-2.3**(1.6)	**-1.5**(1.6)	-0.1(1.9)	-0.1(2.1)
	277	172	149	175	339	390	466	314
SRFP	0.1(1.9)	0.0(1.8)	0.2(1.7)	-0.2(2.0)	**-1.2**(1.9)	-0.6(2.7)	0.2(2.4)	0.0(2.4)
	602	387	388	271	571	659	467	340
EMMA	0.6(1.8)	0.2(2.0)	-0.4(1.4)	-0.2(1.7)	-0.8(1.8)	-1.0(2.0)	-0.1(2.1)	-0.1(2.1)
	400	229	211	222	484	460	453	337

227 **3.2 Pairwise comparisons of XCO$_2$ between algorithms**

228 We made comparisons of geometric and timely matching pairs XCO$_2$ between algorithms in each cell. The pairs of XCO$_2$

229 retrievals were matched between two algorithms timely in the same day, geometrically located within ± 0.01 ° in latitude and

230 longitude. Figure 6 shows pairwise comparisons of XCO$_2$ retrievals between two algorithms that demonstrate the regression

231 slope (a), the coefficient of determination (R^2), the correlation coefficient (r), the number of matching pairs (n) and the biases

232 between every pair of algorithms.

233   It can be seen from Fig. 6 that ACOS generally demonstrates the best agreement with other algorithms (top panel) and

234 the best agreement with EMMA with the greatest correlation of 0.95, a slope of 1.0 and bias of 0.3 ppm among all the

235 pairwise comparisons between algorithms. OCFP generally presents biases larger than 1.4 ppm with other algorithms except

236 for a value of 0.1 ppm compared to NIES. EMMA vs. ACOS and EMMA vs. SRFP present better agreement, with a

237 coefficient of determination greater than 0.87, as EMMA integrates products from seven individual algorithms [Reuter et al.,

238 2013], and the fractions in our study area are 36.7%, 30% and less than 18% from SRFP, ACOS and others, respectively.

239   It can also be seen from the colored points in Fig. 6 that matching pairs of XCO$_2$ for OCFP versus ACOS, SRFP and

240 EMMA mostly concentrated along the 1:1 line in the eastern cells of 105-120 °E (orange and red points) but drifted from the

241 1:1 line in the western cells of 80-100 °E (blue and green points).

242
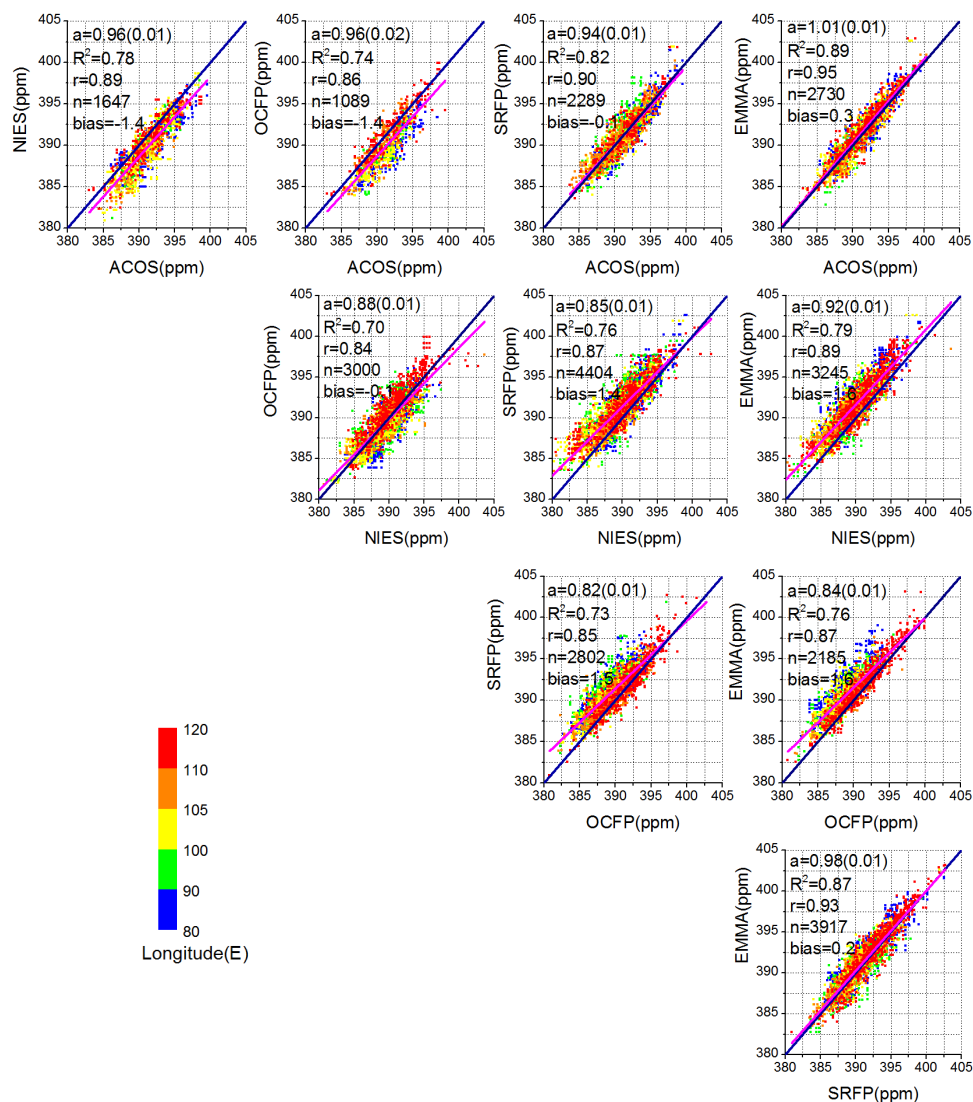
Fig. 6: Algorithm correlation diagrams and statistical characteristics (insets of panels). GOSAT-Y observations were selected over land within ±0.01 °latitude/longitude of each GOSAT-X observation and in the same day. Deep blue solid lines represent a 1:1 line, and the magenta ones display the best fit for all observations. Colored points represent XCO$_2$ for different cells: blue-[80 °E, 90 °E], green-[90 °E, 100 °E], yellow-[100 °E, 105 °E], orange-[105 °E, 110 °E], and red-[110 °E, 120 °E] in the latitude zone [37 °N, 42 °N].

The differences(biases) of matching pairs (the number ranging from 11 to 945) of XCO$_2$ between two algorithms, moreover, were calculated for each cell as shown in Table 3, and the totally averaged absolute differences of matching pairs of XCO$_2$ for an algorithm with the other algorithms were also calculated in each cell as shown in Table 4.

It can be found from Table 3 that the difference is mostly less than 1 ppm in those eastern cells with a longitude greater than 105 °E, and their consistency can be seen in Fig. 6 (red points between 110-120 °E) as well. The differences that are larger than 2 ppm are located in western cells with longitudes less than 105 °E, and these differences are mostly shown in OCFP vs. other algorithms. The total differences shown in Table 4, moreover, indicate that the differences of the five

255 algorithms tend to be similar to the results of matching pairs of XCO_2 (Table 3), and OCFP presents the largest difference up

256 to 2 ppm in the western cells of 80-90 °E.

257 **Table 3. Differences (ppm) between two algorithms (column algorithm minus row algorithm) for each cell, where values in**
258 **parentheses are the corresponding standard deviations.**

	*	NIES	OCFP	SRFP	EMMA	*	NIES	OCFP	SRFP	EMMA
ACOS		-1.4(1.2)	**-2.6**(1.2)	-0.5(1.2)	0.2(1.0)		**-1.6**(1.6)	**-2.0**(1.1)	-0.2(1.2)	0.2(1.1)
NIES	80		-0.9(1.4)	1.1(1.4)	**1.7**(1.5)	100		-0.4(1.4)	1.4(1.5)	**1.6**(1.4)
OCFP	°E			**2.0**(1.2)	**2.6**(1.5)	°E			**1.7**(1.3)	**1.9**(1.4)
SRFP					0.4(1.1)					0.3(1.1)
ACOS		**-2.0**(1.3)	**-1.9**(1.2)	-0.1(1.2)	0.5(0.9)		**-1.6**(1.3)	-0.6(1.4)	0.2(1.2)	0.2(0.9)
NIES	85		-0.4(1.6)	1.5(1.3)	**2.0**(1.5)	105		0.2(1.5)	1.2(1.3)	1.5(1.3)
OCFP	°E			**2.3**(1.4)	**2.7**(1.5)	°E			1.0(1.3)	1.0(1.0)
SRFP					0.2(1.2)					0.2(0.9)
ACOS		-1.2(1.1)	**-1.7**(1.1)	0.8(1.4)	0.5(0.8)		-1.2(1.3)	-0.9(1.4)	0.0(1.4)	0.4(1.1)
NIES	90		-0.8(1.4)	**2.0**(1.4)	1.5(1.2)	110		0.7(1.3)	1.5(1.6)	1.5(1.3)
OCFP	°E			**2.4**(1.5)	**2.0**(1.3)	°E			0.5(1.2)	0.7(1.0)
SRFP					-0.1(1.1)					0.0(1.3)
ACOS		**-3.0**(1.1)	-0.9(1.7)	-0.3(1.2)	0.0(1.1)		-0.6(1.3)	0.1(1.0)	-0.1(1.0)	0.5(1.0)
NIES	95		0.5(2.1)	1.3(2.0)	**1.7**(1.9)	115		0.8(1.5)	0.9(1.3)	1.3(1.5)
OCFP	°E			**1.8**(1.6)	1.4(1.1)	°E			0.2(1.3)	0.5(1.0)
SRFP					0.2(1.3)					0.6(0.9)

259 **The columns labeled with * represent the left longitude of cells (°E).**

260 **Table 4. The average (ppm) of the absolute differences of the target algorithm (in column) matching all other algorithms for each**
261 **cell. Values in parentheses are the corresponding standard deviations.**

Left longitude of cells(°E)	80	85	90	95	100	105	110	115
ACOS	1.5(0.8)	1.4(0.7)	1.2(0.4)	1.6(1.0)	1.4(0.6)	1.1(0.4)	1.1(0.2)	0.9(0.2)
NIES	1.6(0.2)	1.8(0.4)	1.6(0.4)	**2.2**(0.6)	1.6(0.3)	1.5(0.3)	1.5(0.3)	1.3(0.2)
OCFP	**2.2**(0.6)	**2.1**(0.6)	1.9(0.5)	1.7(0.2)	1.7(0.4)	1.2(0.1)	1.1(0.1)	1.0(0.2)
SRFP	1.3(0.5)	1.4(0.7)	1.6(0.8)	1.4(0.6)	1.3(0.5)	1.1(0.3)	1.2(0.4)	1.0(0.2)
EMMA	1.6(0.9)	1.6(1.0)	1.3(0.6)	1.3(0.6)	1.3(0.6)	1.1(0.5)	1.1(0.4)	1.0(0.4)

262

263 To summarize the quantification and analysis in this section, XCO_2 retrievals from three algorithms, ACOS, EMMA and

264 SRFP are mostly consistent, and the bias of ACOS relative to GEOS-Chem is the least among the five algorithms. The

265 difference of XCO_2 from cross-comparing five algorithms likely tends to be less in cells east of 100°E than that in the cells

266 west of 100°E.

Atmospheric
Measurement
Techniques
Discussions

4 Comparison of the spatio-temporal pattern revealed by XCO₂ from the five algorithms and simulation

267

268   We used a combination of sine and cosine trigonometric functions to statistically fit the seasonal variation of XCO_2, which

269 was originally proposed by Keeling et al. (1976) and has been applied extensively in many studies (Thoning et al. 1989;

270 Kulawik et al., 2016; Lindqvist et al., 2015; Zeng et al., 2016; He et al., 2017). Better attributions are thus obtained for XCO_2

271 variation in the seasonal cycle and in spatial background patterns by filtering the noise and filling gaps in the original XCO_2

272 data.

273   First, the monthly averaged XCO_2 was calculated in each cell using XCO_2 retrievals; then, the fit function (Keeling,

274 1976), expressed as the following equation [1], was applied to the monthly averaged XCO_2 from March, 2010 to February,

275 2013 for the five algorithms and GEO-Chem.

276 $$X(t) = A_1 \sin 2\pi t + A_2 \cos 2\pi t + A_3 \sin 4\pi t + A_4 \cos 4\pi t + A_5 + A_6 t \quad [1]$$

277 where t represents elapsed time in years, A_1-A_4 are the coefficients determining the seasonal cycle, A_5 represents the initial

278 state of XCO_2 with seasonal variation removed, which can be regarded as the corresponding background concentration, and

279 A_6 is the slope of the linear part in the yearly increase ignoring the minor non-linear part. To derive A_1-A_6 with the above

280 formula, least squares were applied to fit the input monthly weighted means with the corresponding standard deviations as

281 measures of errors. The monthly weighted means (e.g., X (t)) and the corresponding standard deviations in each cell were

282 calculated with the weights inversely proportional to the square of retrieval uncertainty in each observation point.

283   The accuracy of fitting X(t) depends on the number of gaps in the available XCO_2 retrievals in time and in space

284 resulting from the filtering mechanism for quality controlling. We introduce the Pearson's correlation, hereafter referred to

285 as R, between the input and the predicted results from equation [1] and the unit weight mean square error hereafter referred

286 to as σ, in fitting as an uncertainty to judge whether the fitting results are reasonable or not. In addition, we applied equation

287 [1] to the GEOS-Chem dataset. Since atmospheric transport models do not share the same error sources with satellite-

288 retrieved algorithms and without data gaps, GEOS-Chem provides helpful a priori information for reference.

4.1 Seasonal variation of XCO₂ retrievals

289

290 The time series in each cell are acquired for each algorithm with the above formula [1]. The monthly fitted XCO_2 from

291 March 2010 to February 2013 in each cell for five algorithms as well as GEOS-Chem is shown in Fig. 7. The seasonal

292 amplitudes (the difference between seasonal cycle maximums and minimums) and uncertainty of the fitting function as

293 described by R and σ above are demonstrated in Table 5.

294

Atmospheric
Measurement
Techniques
Open Access
EGU
Discussions

295
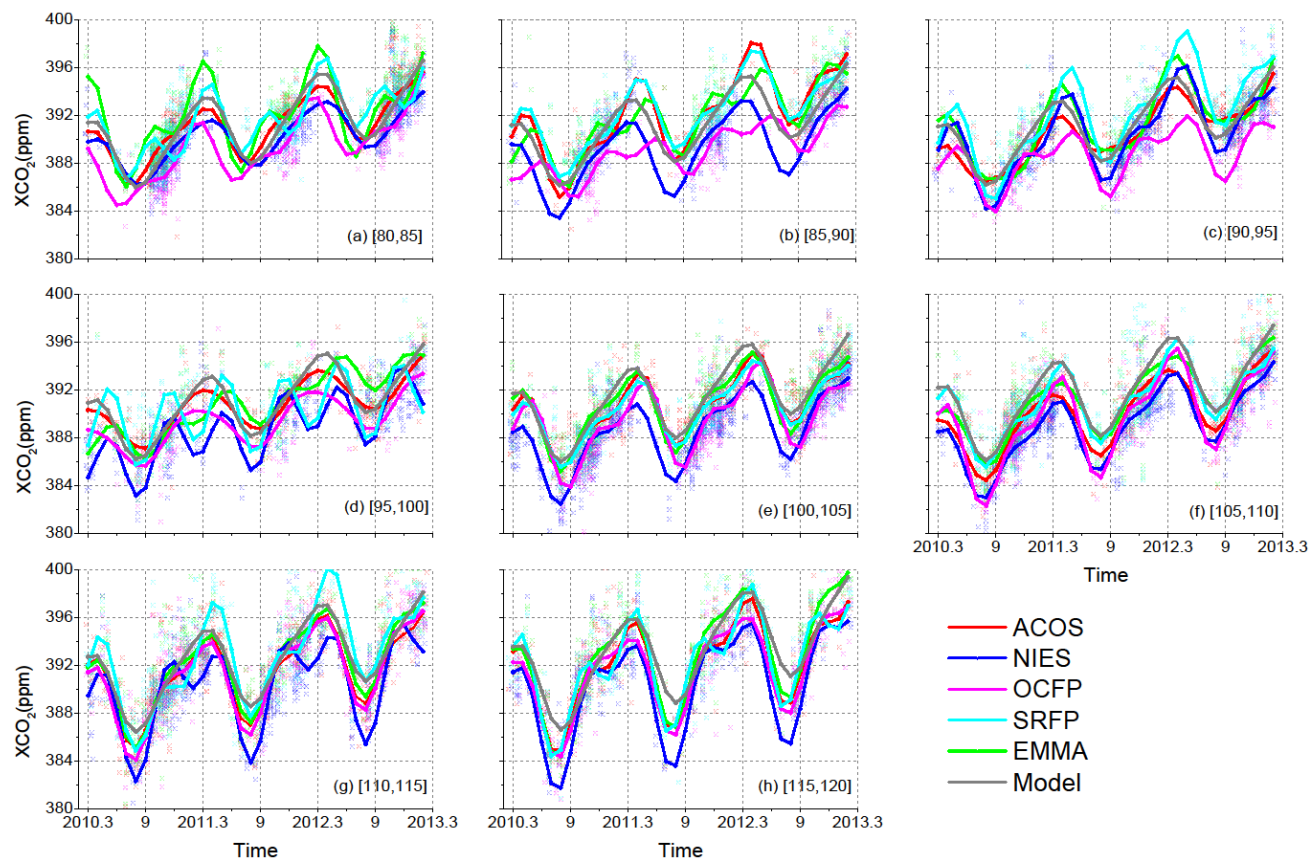
Fig. 7: The time series from March 2010 to February 2013 in eight cells from the western cell of (a) to the eastern end cell of (h), where colored lines represent the fitting seasonal change trend of the five GOSAT-XCO_2 datasets from five algorithms, and the colored points represent single XCO_2 retrievals corresponding to five algorithms according to line color: red is for ACOS, blue for NIES, magenta for OCFP, cyan for SRFP and green for EMMA. The gray line is the fitting seasonal change trend of XCO_2 simulated by GEOS-Chem.

301 **Table 5: Results of fitted seasonal cycle trend and uncertainty of fitting results in each cell for five algorithms and GEOS-Chem,**
302 **The symbols "–" means that filtered results are not available due to large uncertainty judged by R and σ**

Left longitude of cells (°E)	80	85	90	95	100	105	110	115
Seasonal cycle amplitude (ppm)								
ACOSv3.5	5.1	7.8	3.7	4.0	6.6	5.9	8.0	9.3
NIES	4.3	6.9	7.8	-	7.1	6.4	9.5	10.7
OCFP	5.3	3.5	-	3.9	7.7	9.2	8.4	8.6
SRFP	6.3	6.5	8.9	-	5.9	7.4	10.4	10.7
EMMA	-	-	6.6	-	7.3	5.4	8.1	10.1
GEOS-Chem	6.3	5.9	5.7	5.6	6.5	6.9	7.2	7.9
σ(Unit weight mean square error in fitting)(ppm)								
ACOSv3.5	1.2	1.6	1.6	0.6	1.1	1.2	0.4	1.0
NIES	0.7	1.1	1.0	3.0	1.1	1.1	1.5	1.3
OCFP	0.7	0.9	1.5	1.4	1.9	1.1	0.8	0.9
SRFP	1.6	0.7	1.3	3.3	0.8	0.8	1.0	1.0
EMMA	2.7	1.5	1.1	2.1	1.2	0.9	0.6	0.6
GEOS-Chem	0.1	0.1	0.1	0.1	0.1	0.1	0.1	0.1
R (Correlations between fitted XCO2 and monthly averaged original XCO2 in each cell)								
ACOSv3.5	0.92	0.92	0.91	0.95	0.91	0.91	0.98	0.94
NIES	0.89	0.91	0.94	0.68	0.96	0.95	0.89	0.92
OCFP	0.90	0.84	0.79	0.84	0.93	0.93	0.93	0.96
SRFP	0.83	0.94	0.92	0.40	0.95	0.94	0.93	0.90
EMMA	0.84	0.75	0.86	0.78	0.93	0.93	0.97	0.97
GEOS-Chem	1.00	1.00	0.99	0.99	0.99	0.99	0.99	0.99

303

304   Viewing the attribution of XCO_2 in each cell from Fig. 7 and Table 5, we can generally find that the seasonal variations
305 from all XCO_2 retrievals show similar changing trends, except for one extra seasonal cycle maximum being misidentified in
306 some cases mainly due to weaker data constraints for fitting. The timely changing patterns (seasonal cycle phases) of all
307 algorithms demonstrate better agreement in the eastern four cells from 100°E to 115°E than those in the western four cells
308 from 80°E to 95°E.. The correlation coefficients of fitting XCO_2 in Table 5 are also significantly greater in the eastern four
309 cells than those in the western four cells. As a result, the longitude 100°E tends to be a regional border presenting better
310 consistency of XCO_2 among the five algorithms in its eastern cells than those in western cells.

Atmospheric
Measurement
Techniques
Discussions

311   Comparing the five algorithms with GEOS-Chem, one specific result is presented in the eastern-most two cells from

312   110°E to 120°E, in which the seasonal amplitudes of XCO_2 are significantly higher from the five algorithms while the

313   magnitudes of XCO_2 in summer are lower than those from GEOS-Chem as shown in Table 5 and Fig. 7. There is strong CO2

314   absorption from farming activities of wheat and corn in the summer (Lei et al., 2010) and anthropogenic CO_2 emission from

315   extra winter heating in these eastern cells. This result is in agreement with an investigation of results in the whole Chinese

316   mainland (Lei et al., 2014) and at 120-180°E over the globe (Lindqvist et al., 2015), which is likely due to the

317   underestimated widespread bio-ecological CO_2 uptake changes that occurred over the past 50 years in atmospheric transport

318   models (Graven et al., 2013).

319   The XCO_2 values from NIES (blue in Fig. 7) are overall lower than those from the other algorithms, which is due to the

320   uncorrected systematic errors -1.2 ppm (refer to Table 1). The seasonal variations from OCFP (magenta in Fig. 7) are of the

321   overall seasonal changing trend of XCO_2 in cells west of 100°E. The seasonal amplitudes of OCFP presented in Table 5,

322   moreover, are abnormally the lowest in a cell (85-90°E) and the highest in a cell (105-110°E). SRFP and NIES show two

323   abnormal peaks in a cycle of a year in the cell of 95 °E, while some great values of σ and small values of R, shown in bold in

324   Table 5, indicate poor fitting mostly in the same cell (95-110°E). These results are likely induced by large gaps in the

325   available XCO_2 data in time series, which produces a poor fitting constraint.

326   **4.2 Spatio-temporal pattern of detrended XCO_2**

327   We calculated the seasonal averages of the XCO_2 background concentration in each cell after removing the linear yearly

328   increase using the fitting time series of XCO_2 for the five algorithms and GEOS-Chem. The spatio-temporal continuous

329   pattern of background XCO_2 was mapped by Linearly Interpolate Triangulation (Watson et al., 1984) using the seasonal

330   averages of XCO_2 background concentration in each cell for five algorithms and GEOS-Chem, as shown in Fig. 8 (on the

331   left). The spatio-temporal patterns of the differences in XCO_2 between the five algorithms and GEOS-Chem were mapped

332   and are also shown in Fig. 8 (on the right).

Atmospheric
Measurement
Techniques
Discussions

333
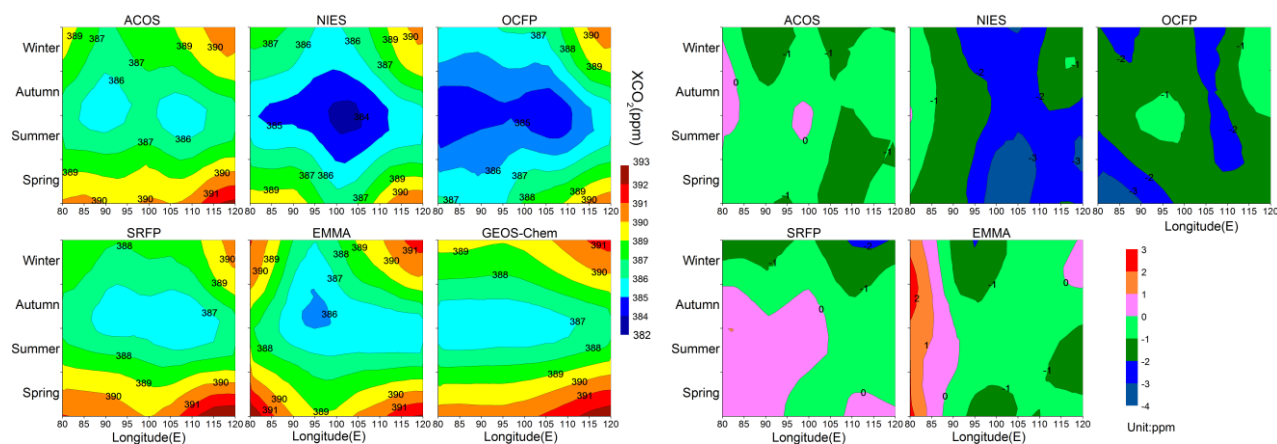
Fig. 8: The spatial (in the study latitude band) and temporal (in seasons) changing patterns of detrended XCO$_2$ from ACOS, EMMA, NIES, OCFP, SRFP and GEOS-Chem (left) and the differences of detrended XCO$_2$ between ACOS, EMMA, NIES, OCFP and SRFP and GEOS-Chem.

It can be seen from Fig. 8 (on the left) that the spatio-temporal patterns from the four algorithms of ACOS, EMMA, NIES and SRFP are generally the same, with an increase spreading outward from the center of each diagram and with the lowest XCO$_2$ located approximately 95 E-105 E and in the period of summer-autumn; meanwhile, OCFP and GEOS-Chem show a similar spatio-temporal pattern where the lowest value is not the center. Two common characteristics of XCO$_2$ spatio-temporal changes from five algorithms and GEOS-Chem can also be found: (1) the seasonal changes of XCO$_2$ are the same in any spatial cells, with lower XCO$_2$ in summer and autumn than that in spring and winter; and (2) spatial changes of XCO$_2$ generally demonstrate larger XCO$_2$ in the eastern cells than those in the western cells in any season.

Compared to those of GEOS-Chem, the spatio-temporal differences of ACOS and SRFP generally demonstrate the smallest values mostly ranging from -1 ppm to 1 ppm. XCO$_2$ values from both NIES and OCFP are lower than GEOS-Chem in space and time, while the XCO$_2$ difference from GEOS-Chem is mostly 1-3 ppm for NIES and 2 ppm for OCFP. As a combination of products including the other four algorithms, EMMA demonstrates the largest difference with GEOS-Chem in most of the western cells in all four seasons where the difference is mostly less than 1 ppm.

To summarize the quantification and analysis in this section, the spatio-temporal pattern of ACOS tends to be inconsistent with SRFP. Figure 8 shows two common characteristics among ACOS, NIES, SRFP and EMMA: (1) XCO$_2$ is lower in summer and autumn but higher in spring and winter. (2) XCO$_2$ is higher west of 90 E and east of 110 E, while it is lower in cells 90 E-110 E. In addition, XCO$_2$ values from NIES and OCFP are lower than those from other algorithms, especially in summer and autumn. A similarly high level is captured by ACOS, EMMA, NIES and SRFP generally in the western deserts with lower CO$_2$ emissions compared to the east, which has abundant emissions. This is distinct from ACOS and EMMA, while OCFP and GEOS-Chem both show an increasing trend from west to east in any season.

Atmospheric
Measurement
Techniques
Discussions

5 Discussion

In this section, an investigation was made into the most likely attribution of regional inconsistency, i.e., aerosols and albedo, and an additional evaluation was made of the latest released ACOS V7.3, the newer version of ACOS data retrieved by the OCO-2 algorithm.

5.1 Discussion of albedo and aerosol effects for XCO_2 retrieval

The above quantification and analyses indicate that generally good agreements are achieved among the five data sets in the eastern cells, while four out of five GOSAT-XCO_2 data sets present abnormal high concentrations in the western cells. It has been known that aerosols are the most important factor inducing errors in satellite-retrieved XCO_2 (Guerlet et al., 2013; Oshchepkov et al., 2013; Yoshida et al., 2013; O'Dell et al., 2012), while Aerosol Optical Depth (AOD) is greatly affected by high surface albedo because of the optical lengthening effect. For that reason, we investigate the spatial and temporal characteristics of aerosols and albedo in our study latitude band to probe the reason why high inconsistency of XCO_2 retrieval algorithms appears in western cells rather than in eastern cells with intensive human activities.

We collected MISR aerosol products (AOD at 555 nm) and GLASS albedo products. The spatial and temporal characteristics of albedo and AOD with seasons in the study area are revealed as shown in Fig. 9, in which they are mapped by the same method as Fig. 8. The seasonal mean AOD and albedo were calculated in spring (MAM), summer (JJA), autumn (SON), and winter (DJF) using the monthly mean AOD and black sky shortwave albedo from January 2010 to December 2012 for every cell.
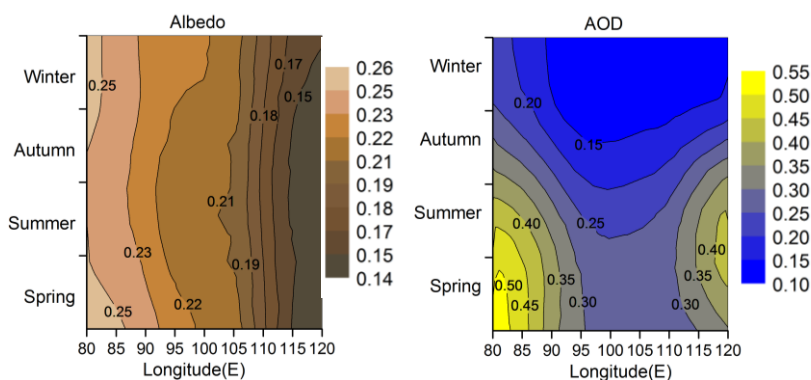
Fig. 9: The temporal and spatial patterns of black sky short wave albedo (left) and aerosol optical depth at 555 nm (right). Colors represent albedo (left) and AOD (right).

Albedo shows little temporal variation with a decreasing trend from west to east as shown in Fig. 9. In contrast with albedo, AOD follows a clear seasonal pattern of a higher level in spring and summer than in autumn and winter. The uplift of AOD in spring and summer is due to the higher frequency of Asian sand and dust storms for cells west of 105 °E. The main contributors to aerosol loading east of 110 °E are emissions from urban fugitive dust/fly ash, dust plumes from deserts in the western and northern China such as the Taklimakan deserts, industrial activities and residential heating (Zhang et al., 2012).

19

Atmospheric
Measurement
Techniques
Discussions

382   The inconsistency of XCO$_2$ from the five algorithms tends to be higher in spring and summer than in autumn and winter

383   in the Taklimakan Deserts in western cells, which is likely the combined effect of high aerosol and high brightness surface

384   (high albedo) on retrieval uncertainty.

385   From the above quantification and analysis, the pairwise differences between OCFP and other algorithms are 1 ppm

386   higher west of 105 °E than east of that, with a difference of 1.6 ppm over the whole study area. The obvious regional

387   characteristic probably relates to the assumption of a cirrus profile according to latitude (GHG-CCI group at University of

388   Leicester, 2014), which is unlikely to be reasonable in our study area. There exists a large amount of high clouds over the

389   Tibetan Plateau (Chen et al., 2005), which is located south of the study cells of 80 °E to 105 °E. The humidity and

390   atmospheric structure are mainly affected by the Tibetan Plateau, and there is a large difference in the cirrus profile between

391   the western cells and the eastern cells over our study area (Wang et al., 2012), which indicates that a uniform profile by

392   latitude will inevitably introduce errors.

393   The pairwise difference between NIES and other algorithms is 1.6 ppm on average, which is distinct among the

394   algorithms. Considering the complicated geographic environment in the study area, this distinct difference is likely related to

395   the presumptions of NIES in aerosol profiles and properties from an aerosol transport model (Table 1), by which cirrus

396   clouds are ignored and little information from observations is used in the retrieving process. Values from EMMA are found

397   to be abnormally large in spring and winter in the western cells from the spatio-temporal patterns (Fig. 8), which is not

398   exactly the same as with the other algorithms. Since data in EMMA are a combination of retrievals from multiple algorithms,

399   it may indicate the uncertainty in all algorithms under the circumstance of high albedo and AOD.

400   With the satellite-observed spectrum used for water and clouds, ACOS sets the initial aerosol types and AOD based on

401   a priori information. On the other hand, SRFP handles aerosol based on the property of number, size and height. Both of the

402   above two mechanisms function well since ACOS and SRFP are generally demonstrated to provide relatively better

403   performance.

404   Noticing that all algorithms differ in simulating scattering in the atmosphere, such as in the aerosol models, the

405   influence of scattering on retrieved XCO$_2$ is too significant to be ignored. Since it is possible for products from different

406   algorithms to agree with each other, there is no denying that satellite XCO$_2$ retrievals have the potential to provide more

407   accurate XCO$_2$ data. Optimization in the handling of aerosol scattering will improve the precision and accuracy of satellite

408   XCO$_2$ retrievals.

409   **5.2 Additional evaluation of the latest released ACOS V7.3**

410   The ACOS/OCO-2 research team released the latest version of the ACOS data ACOS V7.3 during the implementation and

411   completion of this study. We add the cross-comparisons of this version of the data set and other data sets including GEOS-

412   Chem, ACOS V3.5, NIES V02.XX, OCFP 6.0, SRFP V2.3.7 and EMMA V2.1.c in this section. ACOS V7.3 was created by

413   applying the XCO$_2$ retrieval algorithms of OCO-2 to GOSAT. Within the algorithm code of ACOS V3.5, the OCO-2

414   algorithm generating ACOS V7.3 data makes some changes in parameter settings, such as the surface pressure a priori

Atmospheric
Measurement
Techniques
Discussions

415   constraint and cloud ice properties, and it updates the manners of data processing, for example, the bias corrections and

416   filtering mechanism. The available data points, a total of 1980, were shown from March 2010 to February 2013 in Fig. 10,

417   where different colors and symbols in each panel represent the left longitude of cells into which retrievals fall. In cells west

418   of 90 °E, there are a few data points showing abnormal concentrations as high as above 400.0 ppm, which is higher than that

419   of data points in the east, where there are strong anthropogenic CO_2 emissions.
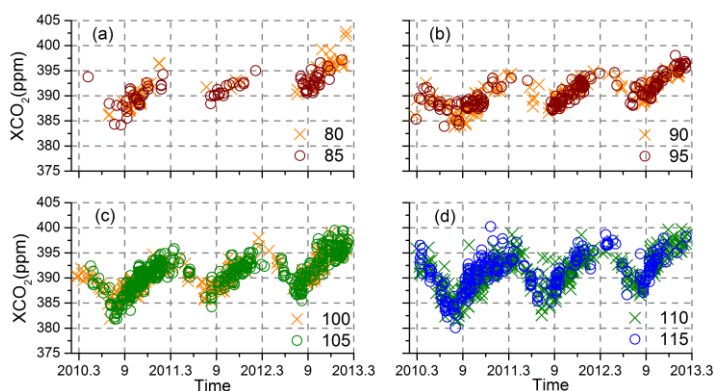
420

421   **Fig. 10. The time series of data points from ACOS V7.3 during the period from March 2010 to February 2013. Different symbols**
422   **in each panel represent the left longitude of the cell into which a data point falls.**

423   We made cross-comparisons between ACOS V7.3 and other data sets. No bias was found in ACOS V7.3 from GEOS-Chem

424   with a standard deviation of 1.6 ppm and R^2=0.77. The comparison results in the cells are shown in Table 6. Generally,

425   ACOS V7.3 is in good agreement with all of them, which is reflected by correlation coefficients r that are above 0.85 and

426   greater than others, as shown in Table 6. The biggest differences up to 3.0 ppm for ACOS V7.3 are found from NIES and

427   OCFP in deserts cells, whereas differences from SRFP and EMMA are mostly within 1.0 ppm. This is similar to ACOS V3.5.

428   The total absolute difference from other algorithms (not including ACOS V3.5) is within 1.0 ppm in cells east of 110 °E but

429   above 2.0 ppm in cells west of 90 °E. It can also be found from Table 6 that the bias of ACOS V7.3 relative to GEOS-Chem

430   is within 0.3 ppm but above 1.3 ppm, in cells east and west of 90 °E, respectively.

431   Compared to the previous version, ACOS V3.5, ACOS V7.3 increases the average by approximately 0.2 ppm. In

432   comparison with the difference patterns with ACOS V3.5, the averages of the absolute differences between ACOS V7.3 and

433   the other four algorithms are similar (<0.1 ppm) and increase by an average of 0.6 ppm (2.1 ppm vs. 1.5 ppm) in cells east of

434   110 °E and west of 90 °E, respectively, while the biases relative to GEOS-Chem decrease approximately 0.3 ppm and increase

435   approximately 0.9 ppm in cells east and west of 90 °E, respectivley.

436   The comparison results further demonstrate inconsistency of XCO_2 among different datasets in the desert cells.

Atmospheric
Measurement
Techniques
Discussions
Open Access

437

Table 6. Differences between ACOS V7.3 and others (including GEOS-Chem and five other algorithms including ACOS V3.5, NIES, OCFP, SRFP and EMMA) in each cell (subtraction from ACOS V7.3). Values in parentheses are the corresponding standard deviations.

Left longitude of cells(°E)	80	85	90	95	100	105	110	115	r
GEOS-Chem	**-1.7**(1.5) 64	-1.3(1.3) 85	0.1(1.2) 167	0.1(1.2) 191	-0.1(1.3) 294	0.3(1.6) 448	0(1.7) 487	0(1.6) 244	0.88
ACOS V3.5	-0.4(0.9) 103	-0.1(1.0) 48	-0.1(1.0) 133	-0.2(1.0) 189	0.0(1.1) 350	-0.5(1.1) 391	0.2(1.2) 244	-0.1(1.1) 126	0.93
NIES	**-3.2**(1.2) 61	**-1.9**(1.5) 100	**-1.6**(1.2) 251	-1.2(1.9) 123	**-1.9**(1.4) 541	**-1.8**(1.5) 317	-1.2(1.6) 397	-0.7(1.5) 277	0.87
OCFP	**-3.1**(1.0) 66	**-3.4**(0.9) 41	**-2.2**(1.1) 157	**-2.5**(1.5) 114	**-2.1**(1.2) 297	-1.5(1.1) 329	-0.5(1.1) 396	-0.1(1.0) 202	0.86
SRFP	-0.8(1.3) 138	-0.7(1.4) 145	0.3(1.3) 345	-0.6(1.3) 337	-0.4(1.3) 466	-0.5(1.4) 631	0.3(1.4) 447	0.1(1.2) 247	0.89
EMMA	-0.3(1.3) 113	-0.5(1.4) 90	0.0(1.0) 190	-0.4(1.4) 241	-0.2(1.3) 405	-0.3(1.2) 383	0.3(1.1) 390	0.5(1.1) 233	0.91
Average absolute difference[1] for four algorithms above	2.2(1.1)	2.0(1.0)	1.4(0.7)	1.7(0.7)	1.6(0.6)	1.4(0.4)	1.1(0.3)	1.0(0.2)	

[1] represents the average of absolute differences of ACOS V7.3 matching other algorithms including NIES, OCFP, SRFP and EMMA for each cell.

6 Conclusion

Although TCCON has been widely accepted as the standard for validation of satellite-based XCO_2 data, it is necessary to better understand the performance of XCO_2 in spatial and timely variations at a regional scale and especially for those regions where ground-based measurements of XCO_2 are not available, such as for the TCCON stations in China. We implement the quantification and assessment of the agreement of multiple algorithms for typical regions with various land covers and enhancement of anthropogenic CO_2 emissions including the megacity of Beijing from 80°E to 120°E in the same latitude band of 40°N to get better knowledge of the regional uncertainty and performance of GOSAT XCO_2 retrievals in China. Regional performance of XCO_2 products from six algorithms (ACOS, NIES, OCFP, SRFP, EMMA, OCO-2) as well as GEOS-Chem simulated XCO_2 are probed to obtain the regional uncertainty and attributions of GOSAT XCO_2 retrievals. In particular, we apply simulated XCO_2 at a high spatial resolution of 0.5° (latitude) x 0.666° (longitude) for a nested grid obtained by GEOS-Chem to assess the regional uncertainty of XCO_2 derived from satellite observations in China. In connection with the inconsistency of algorithms in eight cells, the characteristics of aerosol and albedo are investigated to discuss the further attribution of regional inconsistency of algorithms.

Atmospheric
Measurement
Techniques
Discussions

456   Summarizing the performance of five algorithms (ACOS, NIES, OCFP, SRFP and EMMA) in each cell based on the

457   above quantification and analysis from comparisons with GEOS-Chem, pairwise differences between algorithms and

458   agreement in time series among algorithms, we can obtain the following results in general: (1)The consistency among

459   algorithms is better in the east than in the west as the absolute difference from pairwise comparisons presents values of 0.9-

460   1.5 ppm in eastern cells covered by grassland, cropland and built-up areas and values of 1.2-2.2 ppm in western cells covered

461   by desert with a high-brightness surface;（2）ACOS and SRFP are more satisfying in characterizing spatio-temporal

462   patterns than other algorithms. To conclude, Table 7 presents the regional characteristics and a summary of the results above.

463   **Table 7. Summaries of our analyses above, including uncertainty, emissions, albedo, aerosol optical depth, regional differences in**
464   **footprint retrievals compared to GEOS-Chem, differences in footprint retrievals and agreement in time series among algorithms,**
465   **general differences in footprint retrievals and agreement in detrended XCO_2 compared to GEOS-Chem for algorithms.**

Left longitude of cells (°E)	80	85	90	95	100	105	110	115
CO_2 emissions (Tg/year)[1]	20.1 (24.1)	11.2 (7.8)	1.2 (2.7)	35.8 (20.7)	57.1 (15.6)	515.2 (199.0)	801.3 (600.3)	821.9 (893.3)
Surface type	High brightness desert			Gobi desert		Grassland	Cropland and built-up	
Albedo	0.24-**0.26**	0.23-**0.26**	0.22-0.24	0.19-0.21	0.21-0.22	0.20-0.21	0.15-0.17	0.14-0.16
AOD[2]	0.22-**0.53**	0.16-0.42	0.12-0.32	0.10-0.29	0.12-0.28	0.12-0.28	0.10-0.32	0.10-0.37
Regional Summary in pairwise differences between algorithms	Less Consistency (mean absolute differences 1.2-2.2 ppm) The difference of OCFP is the greatest with most of the other algorithms (1.7-2.2 ppm); next is NIES (1.6-2.2 ppm).					Good consistency (mean absolute differences 0.9-1.5 ppm) ACOS is relatively the least (0.9-1.1 ppm)		
Regional Summary compared to GEOS-Chem	Large biases, of which NIES is the greatest (1.4-3.1 ppm) and next is OCFP (1.2-2.2 ppm)					lesser biases (0.0-0.5 ppm) excluding NIES		
	Similar in seasonal amplitude;					Seasonal amplitude from GEOS-Chem is lower than all of satellite retrieval algorithms.		
Regional pairwise comparisons of ACOS V7.3	Greater biases are presented with OCFP (1.5-3.4 ppm) and NIES (1.2-3.2 ppm)					Lesser biases (0.0-0.5 ppm) excluding NIES		
General differences compared to GEOS-Chem	ACOS presents lowest values (bias -0.1 ppm Std[3] 1.9 ppm), next is SRFP (bias -0.2 ppm Std 2.2 ppm) NIES presents the greatest (bias -2.0 ppm, Std 2.2 ppm).							
Spatio-temporal patterns of XCO_2 compared to GEOS-Chem	ACOS and SRFP are similar to GEOS-Chem. OCFP is in better agreement with GEOS-Chem but the bias is larger.							

466   **[1] represents the total emissions of CO_2 from CHRED (values without parentheses) and from ODIAC (values in parentheses) in**
467   **each cell in 2012. [2] is the range of averaged seasonal aerosol optical depth over a year. [3] is the standard deviation.**

468 The results, indicating that the discrepancies among algorithms are the smallest in eastern cells, which are the strongest

469 anthropogenic emitting source regions in China, implies that the uncertainty of XCO_2 is likely low in this area, which will be

470 sufficiently rigorous for us to apply it to GOSAT XCO_2 in assessment of anthropogenic emissions. Moreover, it was likely

471 that uncertainty in satellite-retrieved XCO_2 is attributed to the combined effects of aerosol and albedo. The large uncertainty

472 of XCO_2 must be improved further, even though many algorithms have endeavored to minimize the effects of aerosol and

473 albedo. With the launch of OCO-2 in 2014 and GOSAT-2 scheduled for 2018, the prospect of a large amount of useful

474 retrieved XCO_2 products is promising. Since low regional XCO_2 biases are necessary for accurately estimating regional

475 carbon sources and sinks, regional uncertainty should be paid more attention in the future.

485 **References**

486 Andres, R. J., Boden, T. A., Bréon, F. M., Ciais, P., Davis, S., Erickson, D., Gregg, J. S., Jacobson, A., Marland, G., Miller,

487 J., Oda, T., Olivier, J. G. J., Raupach, M. R., Rayner, P., and Treanton, K.: A synthesis of carbon dioxide emissions from

488 fossil-fuel combustion, Biogeosciences, 9, 1845-1871, doi:10.5194/bg-9-1845-2012, 2012.

490 Bie, N., Lei, L., He, Z., and Liu, M.: An analysis of atmospheric CO_2 concentration around the takelamagan desert with five

491 products retrieved from satellite observations, International Geoscience and Remote Sensing Symposium, 4087-4089, 2016.

493 Bovensmann, H., Burrows, J. P., Buchwitz, M., Frerick, J., Noël, S.,Rozanov, V. V., Chance, K. V., and Goede, A.:

494 SCIAMACHY –Mission Objectives and Measurement Modes, J. Atmos. Sci., 56,127–150, 1999.

496 Buchwitz, M., Reuter, M., Schneising, O., Boesch, H., Guerlet, S., Dils, B., Aben, I., Armante, R., Bergamaschi, P.,

497 Blumenstock, T., Bovensmann, H., Brunner, D., Buchmann, B., Burrows, J. P., Butz, A., Chédin, A., Chevallier, F.,

498 Crevoisier, C. D., Deutscher, N. M., Frankenberg, C., Hase, F., Hasekamp, O. P., Heymann, J., Kaminski, T., Laeng, A.,

499 Lichtenberg, G., De Mazière, M., Noël, S., Notholt, J., Orphal, J., Popp, C., Parker, R., Scholze, M., Sussmann, R., Stiller, G.

Atmospheric
Measurement
Techniques
Discussions

Open Access

EGU

500 P., Warneke, T., Zehner, C., Bril, A., Crisp, D., Griffith, D. W. T., Kuze, A., O'Dell, C., Oshchepkov, S., Sherlock, V., Suto,
501 H., Wennberg, P., Wunch, D., Yokota, T., and Yoshida, Y.: The Greenhouse Gas Climate Change Initiative (GHG-CCI):
502 Comparison and quality assessment of near-surface-sensitive satellite-derived CO2 and CH4 global data sets, Remote
503 Sensing of Environment, 162, 344-362, doi:10.1016/j.rse.2013.04.024, 2015.
504
505 Buchwitz, M., B. Dils, H. Boesch, C. Crevoisier, R. Detmers, C. Frankenberg, O. Hasekamp, W. Hewson, A. Laeng , S.
506 Noel, J. Notholt, R. Parker, M. Reuter & O. Schneising. ESA Climate Change Initiative (CCI) Product Validation and
507 Intercomparison Report (PVIR) for the Essential Climate Variable (ECV) Greenhouse Gases (GHG), http://www.iup.uni-
508 bremen.de/sciamachy/NIR_NADIR_WFM_DOAS/crdp3_main.html , 2016.
509
510 Burrows, J. P., Hölzle, E., Goede, A. P. H., Visser, H., and Fricke,W.: SCIAMACHY – Scanning Imaging Absorption
511 Spectrometerfor Atmospheric Chartography, Acta Astronaut., 35, 445–451,1995.
512
513 Butz, A., Guerlet, S., Hasekamp, O., Schepers, D., Galli, A., Aben, I., Frankenberg, C., Hartmann, J. M., Tran, H., Kuze, A.,
514 Keppel-Aleks, G., Toon, G., Wunch, D., Wennberg, P., Deutscher, N., Griffith, D., Macatangay, R., Messerschmidt, J.,
515 Notholt, J., and Warneke, T.: Toward accurate CO2and CH4observations from GOSAT, Geophysical Research Letters, 38,
516 n/a-n/a, doi:10.1029/2011gl047888, 2011.
517
518 Cai, B., and Zhang, L.: Urban CO2 emissions in China: Spatial boundary and performance comparison, Energy Policy, 66,
519 557-567, doi:10.1016/j.enpol.2013.10.072, 2014.
520
521 Chen, B.: Seasonal migration of cirrus clouds over the Asian Monsoon regions and the Tibetan Plateau measured from
522 MODIS/Terra, Geophysical Research Letters, 32, doi:10.1029/2004gl020868, 2005.
523
524 Ciais, P., Rayner, P., Chevallier, F., Bousquet, P., Logan, M., Peylin, P., and Ramonet, M.: Atmospheric inversions for
525 estimating CO2 fluxes: methods and perspectives, Climatic Change, 103, 69-92, doi:10.1007/s10584-010-9909-3, 2010.
526
527 Cogan, A. J., Boesch, H., Parker, R. J., Feng, L., Palmer, P. I., Blavier, J. F. L., Deutscher, N. M., Macatangay, R., Notholt,
528 J., Roehl, C., Warneke, T., and Wunch, D.: Atmospheric carbon dioxide retrieved from the Greenhouse gases Observing
529 SATellite (GOSAT): Comparison with ground-based TCCON observations and GEOS-Chem model calculations, Journal of
530 Geophysical Research: Atmospheres, 117, n/a-n/a, doi: 10.1029/2012jd018087, 2012.
531
532 Connor, B. J., Boesch, H., Toon, G., Sen, B., Miller, C., and Crisp, D.: Orbiting Carbon Observatory: Inverse method and
533 prospective error analysis, Journal of Geophysical Research: Atmospheres, 113, n/a-n/a,doi:10.1029/2006jd008336, 2008.

534

535 Crisp, D., Atlas, R. M., Br ′ eon, F.-M., Brown, L. R., Burrows, J. P.,Ciais, P., Connor, B. J., Doney, S. C., Fung, I. Y.,

536 Jacob, D. J.,Miller, C. E., O'Brien, D., Pawson, S., Randerson, J. T., Rayner, P., Salawitch, R. S., Sander, S. P., Sen, B.,

537 Stephens, G. L., Tans,P. P., Toon, G. C., Wennberg, P. O., Wofsy, S. C., Yung, Y. L.,Kuang, Z., Chudasama, B., Sprague,

538 G., Weiss, P., Pollock, R.,Kenyon, D., and Schroll, S.: The Orbiting Carbon Observatory(OCO) mission, Adv. Space Res.,

539 34, 700–709, 2004.

540

541 Detmers, R., Hasekamp, O.: Product User Guide (PUG) for the RemoTeC XCO2 Full Physics GOSAT Data Product,

542 http://www.esa-ghg-cci.org/sites/default/files/documents/public/documents/GHG-CCI_DATA.html , 2015.

543

544 Goddard Earth Science Data Information and Services Center (GES DISC): ACOS Level 2 Standard Product Data User's

545 Guide, v3.5, http://co2.jpl.nasa.gov ,2016.

546

547 Goddard Earth Science Data Information and Services Center (GES DISC): ACOS Level 2 Standard Product Data User's

548 Guide, v7.3, http://co2.jpl.nasa.gov , 2017.

549

550 Giglio, L., Randerson, J. T., and van der Werf, G. R.: Analysis of daily, monthly, and annual burned area using the fourth-

551 generation global fire emissions database (GFED4), Journal of Geophysical Research: Biogeosciences, 118, 317-328,

552 doi:10.1002/jgrg.20042, 2013.

553

554 Graven, H. D., Keeling, R. F., Piper, S. C., Patra, P. K., Stephens, B. B., Wofsy, S. C., Welp, L. R., Sweeney, C., Tans, P. P.,

555 Kelley, J. J., Daube, B. C., Kort, E. A., Santoni, G. W., and Bent, J. D.: Enhanced seasonal exchange of CO2 by northern

556 ecosystems since 1960, Science, 341, 1085-1089, doi:10.1126/science.1239207, 2013.

557

558 Guan, D., Liu, Z., Geng, Y., Lindner, S., and Hubacek, K.: The gigatonne gap in China/'s carbon dioxide inventories, Nature

559 Clim. Change, 2, 672-675, doi:10.1038/nclimate1560, 2012.

560

561 Guerlet, S., Butz, A., Schepers, D., Basu, S., Hasekamp, O. P., Kuze, A., Yokota, T., Blavier, J. F., Deutscher, N. M.,

562 Griffith, D. W. T., Hase, F., Kyro, E., Morino, I., Sherlock, V., Sussmann, R., Galli, A., and Aben, I.: Impact of aerosol and

563 thin cirrus on retrieving and validating XCO2from GOSAT shortwave infrared measurements, Journal of Geophysical

564 Research: Atmospheres, 118, 4887-4905, doi:10.1002/jgrd.50332, 2013.

565

566   GHG-CCI group at University of Leicester: Algorithm Theoretical Basis Document Version 3 (ATBDv3)-The University of

567   Leicester Full-Physics Retrieval Algorithm for the retrieval of XCO2 and XCH4, http://www.esa-ghg-

568   cci.org/sites/default/files/documents/public/documents/GHG-CCI_DATA.html , 2014.

569

570   Hasekamp, O. H., Haili, Detmers,Rob, Butz,Andre: ESA Climate Change Initiative (CCI) Algorithm Theoretical Basis

571   Document for the RemoTeC XCO2 and XCH4 Full Physics Products of the Essential Climate Variable (ECV) Greenhouse

572   Gases (GHG), http://www.esa-ghg-cci.org/sites/default/files/documents/public/documents/GHG-CCI_DATA.html, 2015.

573

574   He, Z., Zeng, Z.-C., Lei, L., Bie, N., and Yang, S.: A Data-Driven Assessment of Biosphere-Atmosphere Interaction Impact

575   on Seasonal Cycle Patterns of XCO2 Using GOSAT and MODIS Observations, Remote Sensing, 9, 251,

576   doi:10.3390/rs9030251, 2017.

577

578   Hewson, W.: Product User Guide:University of Leicester full-physics XCO2 retrieval algorithm for CRDP3 – OCFP v6.0,

579   http://www.esa-ghg-cci.org/sites/default/files/documents/public/documents/GHG-CCI_DATA.html ,2016.

580

581   Keeling, C. D., Bacastow, R. B., Bainbridge, A. E., Ekdahl Jr., C. A., Guenther, P. R., Waterman, L. S., and Chin, J. F. S.:

582   Atmospheric carbon dioxide variations at Mauna Loa Observatory, Hawaii, Tellus A, 28, 10.3402/tellusa.v28i6.11322, 2011.

583

584   Keller, C. A., Long, M. S., Yantosca, R. M., Da Silva, A. M., Pawson, S., and Jacob, D. J.: HEMCO v1.0: a versatile,

585   ESMF-compliant component for calculating emissions in atmospheric models, Geoscientific Model Development, 7, 1409-

586   1417, doi:10.5194/gmd-7-1409-2014, 2014.

587

588   Kulawik, S., Wunch, D., apos, Dell, C., Frankenberg, C., Reuter, M., Oda, T., Chevallier, F., Sherlock, V., Buchwitz, M.,

589   Osterman, G., Miller, C. E., Wennberg, P. O., Griffith, D., Morino, I., Dubey, M. K., Deutscher, N. M., Notholt, J., Hase, F.,

590   Warneke, T., Sussmann, R., Robinson, J., Strong, K., Schneider, M., De Mazière, M., Shiomi, K., Feist, D. G., Iraci, L. T.,

591   and Wolf, J.: Consistent evaluation of ACOS-GOSAT, BESD-SCIAMACHY, CarbonTracker, and MACC through

592   comparisons to TCCON, Atmospheric Measurement Techniques, 9, 683-709, doi:10.5194/amt-9-683-2016, 2016.

593

594   Lei, H., and Yang, D.: Seasonal and interannual variations in carbon dioxide exchange over a cropland in the North China

595   Plain, Global change biology, 16, 2944-2957, doi:10.1111/j.1365-2486.2009.02136.x, 2010.

596

597   Lei, L., Guan, X., Zeng, Z., Zhang, B., Ru, F., and Bu, R.: A comparison of atmospheric CO2 concentration GOSAT-based

598   observations and model simulations, Science China Earth Sciences, 57, 1393-1402, doi:10.1007/s11430-013-4807-y, 2014.

599

600 Lindqvist, H., O'Dell, C. W., Basu, S., Boesch, H., Chevallier, F., Deutscher, N., Feng, L., Fisher, B., Hase, F., Inoue, M.,
601 Kivi, R., Morino, I., Palmer, P. I., Parker, R., Schneider, M., Sussmann, R., and Yoshida, Y.: Does GOSAT capture the true
602 seasonal cycle of carbon dioxide?, Atmospheric Chemistry and Physics, 15, 13023-13040, doi:10.5194/acp-15-13023-2015,
603 2015.

604

605 Liu, D., Lei, L., Guo, L., and Zeng, Z.-C.: A Cluster of CO2 Change Characteristics with GOSAT Observations for Viewing
606 the Spatial Pattern of CO2 Emission and Absorption, Atmosphere, 6, 1695-1713, doi:10.3390/atmos6111695, 2015.

607

608 Liu, Q., Wang, L., Qu, Y., Liu, N., Liu, S., Tang, H., and Liang, S.: Preliminary evaluation of the long-term GLASS albedo
609 product, International Journal of Digital Earth, 6, 69-95, 2013.

610

611 Liu, Y., and Yang, D.: Advancements in theory of GHG observation from space, Science Bulletin, 61, 349-352,
612 doi:10.1007/s11434-016-1022-1, 2016.

613

614 Liu, Z., Guan, D., Wei, W., Davis, S. J., Ciais, P., Bai, J., Peng, S., Zhang, Q., Hubacek, K., Marland, G., Andres, R. J.,
615 Crawford-Brown, D., Lin, J., Zhao, H., Hong, C., Boden, T. A., Feng, K., Peters, G. P., Xi, F., Liu, J., Li, Y., Zhao, Y., Zeng,
616 N., and He, K.: Reduced carbon emission estimates from fossil fuel combustion and cement production in China, Nature,
617 524, 335-338, doi:10.1038/nature14677, 2015.

618

619

620 Messerschmidt, J., Parazoo, N., Wunch, D., Deutscher, N. M., Roehl, C., Warneke, T., and Wennberg, P. O.: Evaluation of
621 seasonal atmosphere–biosphere exchange estimations with TCCON measurements, Atmospheric Chemistry and Physics, 13,
622 5103-5115, doi:10.5194/acp-13-5103-2013, 2013.

623

624 Nassar, R., Jones, D. B. A., Suntharalingam, P., Chen, J. M., Andres, R. J., Wecht, K. J., Yantosca, R. M., Kulawik, S. S.,
625 Bowman, K. W., Worden, J. R., Machida, T., and Matsueda, H.: Modeling global atmospheric CO_2 with
626 improved emission inventories and CO_2 production from the oxidation of other carbon species, Geoscientific
627 Model Development, 3, 689-716, doi:10.5194/gmd-3-689-2010, 2010.

628

629 Nassar, R., Napier-Linton, L., Gurney, K. R., Andres, R. J., Oda, T., Vogel, F. R., and Deng, F.: Improving the temporal and
630 spatial distribution of CO2emissions from global fossil fuel emission data sets, Journal of Geophysical Research:
631 Atmospheres, 118, 917-933, doi:10.1029/2012jd018196, 2013.

632

633   National Institute for Environmental Studies, GOSAT Project Office: NIES GOSAT TANSO-FTS SWIR Level 2 Data

634   Product Format Description Version 2.50, https://data2.gosat.nies.go.jp/doc/document.html#Document , 2015.

635

636   Oda, T., and Maksyutov, S.: A very high-resolution (1 km×1 km) global fossil fuel CO_2 emission inventory

637   derived using a point source database and satellite observations of nighttime lights, Atmospheric Chemistry and Physics, 11,

638   543-556, doi:10.5194/acp-11-543-2011, 2011.

639

640   O'Dell, C. W., Connor, B., Bösch, H., O'Brien, D., Frankenberg, C., Castano, R., Christi, M., Eldering, D., Fisher, B.,

641   Gunson, M., McDuffie, J., Miller, C. E., Natraj, V., Oyafuso, F., Polonsky, I., Smyth, M., Taylor, T., Toon, G. C., Wennberg,

642   P. O., and Wunch, D.: The ACOS CO_2 retrieval algorithm – Part 1: Description and validation against

643   synthetic observations, Atmospheric Measurement Techniques, 5, 99-121, doi:10.5194/amt-5-99-2012, 2012.

644

645   Oshchepkov, S., Bril, A., Yokota, T., Wennberg, P. O., Deutscher, N. M., Wunch, D., Toon, G. C., Yoshida, Y., O'Dell, C.

646   W., Crisp, D., Miller, C. E., Frankenberg, C., Butz, A., Aben, I., Guerlet, S., Hasekamp, O., Boesch, H., Cogan, A., Parker,

647   R., Griffith, D., Macatangay, R., Notholt, J., Sussmann, R., Rettinger, M., Sherlock, V., Robinson, J., Kyrö, E., Heikkinen, P.,

648   Feist, D. G., Morino, I., Kadygrov, N., Belikov, D., Maksyutov, S., Matsunaga, T., Uchino, O., and Watanabe, H.: Effects of

649   atmospheric light scattering on spectroscopic observations of greenhouse gases from space. Part 2: Algorithm

650   intercomparison in the GOSAT data processing for CO2retrievals over TCCON sites, Journal of Geophysical Research:

651   Atmospheres, 118, 1493-1512, doi:10.1002/jgrd.50146, 2013.

652

653   Osterman, G. E., Annmarie;Avis, Charles ; O'Dell, Christopher ; Martinez, Elmain; Elmain; Crisp, Elmain; Frankenberg,

654   Christian; Fisher, Brendan: ACOS Level 2 Standard Product Data User's Guide, v3.5, 2016.

655

656   Osterman, G. E., Annmarie;Avis, Charles ; O'Dell, Christopher ; Martinez, Elmain; Elmain; Crisp, Elmain; Frankenberg,

657   Christian; Fisher, Brendan: ACOS Level 2 Standard Product Data User's Guide, v7.3, 2017.

658

659   Reuter, M., Bösch, H., Bovensmann, H., Bril, A., Buchwitz, M., Butz, A., Burrows, J. P., O'Dell, C. W., Guerlet, S.,

660   Hasekamp, O., Heymann, J., Kikuchi, N., Oshchepkov, S., Parker, R., Pfeifer, S., Schneising, O., Yokota, T., and Yoshida,

661   Y.: A joint effort to deliver satellite retrieved atmospheric CO_2 concentrations for surface flux inversions: the

662   ensemble median algorithm EMMA, Atmospheric Chemistry and Physics, 13, 1771-1780, doi:10.5194/acp-13-1771-2013,

663   2013.

664

665   Takahashi, T., Sutherland, S. C., Wanninkhof, R., Sweeney, C., Feely, R. A., Chipman, D. W., Hales, B., Friederich, G.,

666   Chavez, F., and Sabine, C.: Takahashi, T. et al. Climatological mean and decadal changes in surface ocean pCO2, and net

Atmospheric
Measurement
Techniques
Discussions

667 sea-air CO2 flux over the global oceans. Deep-Sea Res. II 56, 554-577, Deep Sea Research Part II Topical Studies in
668 Oceanography, 56, 554-577, 2009.

669

670 Thoning, K. W., Tans, P. P., and Komhyr, W. D.: Atmospheric carbon dioxide at Mauna Loa Observatory: 2. Analysis of the
671 NOAA GMCC data, 1974–1985, Journal of Geophysical Research Atmospheres, 94, 8549-8565, 1989.

672

673 Wang, J., Cai, B., Zhang, L., Cao, D., Liu, L., Zhou, Y., Zhang, Z., and Xue, W.: High resolution carbon dioxide emission
674 gridded data for China derived from point sources, Environmental science & technology, 48, 7085-7093,
675 doi:10.1021/es405369r, 2014.

676

677 Wang, Min-zhong, H. Q., Wei Wen-shou, Yang Lian-mei, and Zhao Yong: Observational Analysis of the Troposphere and
678 Low Stratosphere at Minfeng Station in the North Side of the Tibetan Plateau in July 2011, Plateau Meteorology, 31, 12,
679 2012.

680

681 Wang, W., Liu, C., Liu, W., Xie, P., Liu, J., Sun, Y., Tian, Y., Xu, J., Morino, I., Velazco, V. A., and Griffith, D. W. T.:
682 Investigating the performance of a greenhouse gas observatory in Hefei, China, Atmospheric Measurement Techniques
683 Discussions, 1-26, doi: 10.5194/amt-2016-296, 2016.

684

685

686 Watson, D. F., and Philip, G. M.: Triangle based interpolation, Journal of the International Association for Mathematical
687 Geology, 16, 779-795, doi:10.1007/BF01036704, 1984.

688

689 Wunch, D., Wennberg, P. O., Toon, G. C., Connor, B. J., Fisher, B., Osterman, G. B., Frankenberg, C., Mandrake, L., O'Dell,
690 C., Ahonen, P., Biraud, S. C., Castano, R., Cressie, N., Crisp, D., Deutscher, N. M., Eldering, A., Fisher, M. L., Griffith, D.
691 W. T., Gunson, M., Heikkinen, P., Keppel-Aleks, G., Kyrö, E., Lindenmaier, R., Macatangay, R., Mendonca, J.,
692 Messerschmidt, J., Miller, C. E., Morino, I., Notholt, J., Oyafuso, F. A., Rettinger, M., Robinson, J., Roehl, C. M., Salawitch,
693 R. J., Sherlock, V., Strong, K., Sussmann, R., Tanaka, T., Thompson, D. R., Uchino, O., Warneke, T., and Wofsy, S. C.: A
694 method for evaluating bias in global measurements of CO_2 total columns from space, Atmospheric Chemistry
695 and Physics, 11, 12317-12337, doi:10.5194/acp-11-12317-2011, 2011.

696

697 Yokota, T., Oguma, H., Morino, I., and Inoue, G.: A nadir looking SWIR sensor to monitor CO2 column density for
698 Japanese GOSAT project, Proceedings of the twenty-fourth international symposium on space technology and science,
699 Miyazaki: Japan Society for Aeronautical and Space Sciences and ISTS, 887–889, 2004.

700

Atmospheric
Measurement
Techniques
Discussions

Open Access

EGU

701   Yoshida, Y., Kikuchi, N., Morino, I., Uchino, O., Oshchepkov, S., Bril, A., Saeki, T., Schutgens, N., Toon, G. C., Wunch, D.,
702   Roehl, C. M., Wennberg, P. O., Griffith, D. W. T., Deutscher, N. M., Warneke, T., Notholt, J., Robinson, J., Sherlock, V.,
703   Connor, B., Rettinger, M., Sussmann, R., Ahonen, P., Heikkinen, P., Kyrö, E., Mendonca, J., Strong, K., Hase, F., Dohe, S.,
704   and Yokota, T.: Improvement of the retrieval algorithm for GOSAT SWIR XCO_2 and XCH_4 and
705   their validation using TCCON data, Atmospheric Measurement Techniques, 6, 1533-1547, doi:10.5194/amt-6-1533-2013,
706   2013.
707
708   Zeng, Z.-C., Lei, L., Strong, K., Jones, D. B. A., Guo, L., Liu, M., Deng, F., Deutscher, N. M., Dubey, M. K., Griffith, D. W.
709   T., Hase, F., Henderson, B., Kivi, R., Lindenmaier, R., Morino, I., Notholt, J., Ohyama, H., Petri, C., Sussmann, R., Velazco,
710   V. A., Wennberg, P. O., and Lin, H.: Global land mapping of satellite-observed CO2total columns using spatio-temporal
711   geostatistics, International Journal of Digital Earth, 1-31, doi:10.1080/17538947.2016.1156777, 2016.
712
713   Zhang, X. Y., Wang, Y. Q., Niu, T., Zhang, X. C., Gong, S. L., Zhang, Y. M., and Sun, J. Y.: Atmospheric aerosol
714   compositions in China: spatial/temporal variability, chemical signature, regional haze distribution and comparisons with
715   global aerosols, Atmospheric Chemistry and Physics, 12, 779-799, doi:10.5194/acp-12-779-2012, 2012.
716
717